Surfaces and Interfaces 68 (2025) 106666

Contents lists available at ScienceDirect

Surfaces and Interfaces

journal homepage: www.sciencedirect.com/journal/surfaces-and-interfaces

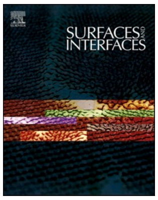

Laser-induced p- and n-type graphene composites for flexible electronics

Ilia Petrov [a], Dmitry Cheshev [a], Sergey Kaprov [a], Fedora Vasileva [b], Raul D. Rodriguez [a,*], Evgeniya Sheremet [a]

[a] Tomsk Polytechnic University, Lenin Ave. 30, Tomsk, 634050, Russia
[b] M.K. Ammosov North-Eastern Federal University, Belinsky str 58, Yakutsk, 677000, Russia

ARTICLE INFO

Keywords:
Reduced graphene
Laser processing
Conductivity type
Composite
Polymer
Flexible electronics

ABSTRACT

Graphene-based technologies have rapidly developed in the last decades, evolving from theoretical concepts to multifunctional devices. However, controlling graphene's electronic properties, e.g., type of conductivity or bandgap, is still in demand and critical to designing advanced flexible electronics. In this work, we demonstrate precise control over the semiconducting properties of reduced graphene oxide, enabling the fabrication of p- and n-type graphene composites via laser processing of graphene oxide (GO) and mildly oxidized graphene (MOG) on polymers. The control of graphene functionalization during the synthesis allowed the manufacturing of conductive composites with predictable conductivity type and sheet resistance below 35 Ohm sq^{-1}. Our results also reveal the significant role of the substrate for laser processing, determining the conductivity type of the final composite. We demonstrate the applicability of laser-processed p-n junctions in flexible thermocouples with tunable sensitivity from 15 to 19 μV K^{-1}. The p- and n-type composites were successfully integrated as channel materials for electrolyte-gated transistors (EGTs) with up to 150 μS transconductance. Notably, the EGTs demonstrate ambipolar behavior with reversible p- to n-transition during operation due to ion doping. These findings expand the capabilities of laser-processed graphene/polymer composites and, for the first time, demonstrate electrochemical doping of reduced graphene-based transistors within the water window and fabricate stable reduced graphene/polymer liquid-gated transistors with an n-type channel.

1. Introduction

Flexible electronics (FE) is a relatively young trend that emerged in the early 2000s. It includes electrical circuits and devices that can be deformed without irreversible degradation of electronic properties. Thanks to Geim and Novoselov [1], the discovery of graphene revolutionized material science. It launched a new era in carbon electronic materials, and the carbon nanomaterials appeared to be perfectly adapted to FE applications. Despite graphene's superior mechanical, electrical, optical, and thermal properties, it is still hard to produce and manipulate, and it lacks a bandgap [2] that limits its application in electronics. For instance, the zero bandgap results in poor on-off current ratios in field-effect transistors [2] and weak light-matter interaction in photonic devices [3]. Because of that, different forms of functionalized graphene, such as graphene oxide (GO) [4,5], modified graphene [6], mildly oxidized graphene [7], *etc.*, were proposed in the literature. Facile production, low cost, better solvent dispersibility, and the possibility of tuning the bandgap and restoring electrical conductivity following the transformation to reduced graphene oxide (rGO) make GO highly attractive for designing electronic circuits and devices [8]. GO reduction methods include thermal, chemical, optical, and other approaches [9]. In our research, we found that laser processing of GO on a polymer substrate could provide both reduction and integration of rGO into the polymer matrix by forming a conductive composite in a single process without additional substrate modification [10]. This method completely fulfills the requirements of FE: electrical conductivity, flexibility, and mechanical stability. Moreover, a PC-controlled laser engraver allows the design of circuits at the micrometer scale. Using laser processing, it is possible to fabricate robust and flexible (bio)sensors, electrochemical/bio electrodes, and antennas [6,11,12].

Nevertheless, most electronic circuits require semiconducting materials whose conductivity can be modulated, as well as elements with p- and n-type conductivity and their junctions [13]. Their fabrication is challenging for carbon electronics, especially for laser-processed structures. The conductivity type of carbon materials depends on various factors like water/oxygen adsorption [14,15], doping, and processing

---

* Corresponding author.
E-mail address: raul@tpu.ru (R.D. Rodriguez).

https://doi.org/10.1016/j.surfin.2025.106666
Received 27 January 2025; Received in revised form 22 April 2025; Accepted 8 May 2025

conditions. For instance, nitrogen doping of graphene, rGO, and carbon nanotubes results in the rise of n-type conductivity [16–18], while adsorbed oxygen groups lead to p-doping of graphene [19]. Thus, it is possible to obtain p- or n-type rGO by controlling the concentration of electron-withdrawing or electron-donating oxygen-containing groups. It was demonstrated by Nguyen et al. [20] who converted between p- and n-type rGO by controlling the annealing temperature, which removed the functional groups. Also, p- and n-type rGO materials were obtained using a femtosecond pulsed laser with different energy densities [21]. At the same time, it was established that rGO contains both charge carriers, holes and electrons, which is reflected in a typical ambipolar behavior of rGO electrolyte-gated transistors [22]. However, to our knowledge, there are no reports on controlling the conductivity type of carbon/polymer composites essential for FE. Moreover, the heat sensitivity of many flexible substrates limits the processing temperature, driving us to look for other ways to control the carbon/polymer composite conductivity type while maintaining low process temperatures.

In this work, for the first time, we demonstrate the effect of the initial carbon precursor functionalization on the conductivity type of carbon-based composites. We laser-processed two carbon materials, GO and mildly oxidized graphene (MOG) [7], resulting in p- and n-type composite structures and a p-n junction. We investigated the physicochemical properties, including Hall measurements and Seebeck coefficient. We verified the origin of p-/n-type conductivity with XPS and demonstrated its application in flexible electronics. The possibility of creating p- and n-type carbon/polymer composite structures within low-temperature processes is essential for FE technology. To illustrate this approach's versatility and practical potential, we fabricated a flexible electrolyte-gated transistor and thermocouple using the same laser processing regime for GO and MOG films on PET.

2. Experimental section

2.1. Fabrication of conductive structures

2.1.1. GO/PET fabrication

4 mg/mL water dispersion of GO (Graphenea, Spain) was dropcast on a 0.65-mm-thick PET sheet with an areal density of 100 μL/cm^2 and dried in the hood at room temperature.

2.1.2. MOG/PET fabrication

MOG was synthesized using electrochemical exfoliation of graphite in a 0.15 M aqueous solution of ammonium sulfate followed by ultrasonic treatment. Gold was used as a cathode, and a voltage of 15 V was applied for 15 min. The details can be found in the previous work [23]. A 6 mg/mL water dispersion of MOG was drop cast on a 0.65-mm-thick PET sheet with an areal density of 180 μL/cm^2 and dried on a heating plate at 50 °C.

2.1.3. Laser processing

The laser processing was performed using a 3 W computer-controlled pulsed 438 nm laser. The pulse energy was 175 mJ, the pulse frequency was 2.8 kHz, and the pulse duration was 250 μs. Finally, the samples were washed with water in a 120 W ultrasound bath for 2 min.

2.2. Characterization and applications

2.2.1. Conductivity type, surface charge density, charge mobility, and sheet resistance data were collected using the Hall effect measurement system HMS5000/AMP55 (Ecopia, South Korea).

2.2.2. Scanning electron microscopy images were obtained using Coxem EM-30 scanning electron microscope (Coxem, Korea).

2.2.3. Raman spectra were collected using confocal Raman microscopy (NTEGRA Spectra, NT-MDT, Zelenograd, Russia). A 532 nm laser was used for sample characterization using a 20x objective. Exposure time and laser power on the sample were equal to 5 min and 30 μW, respectively.

2.2.4. FTIR spectra were collected in transmission mode using IRAffinity-1S (Shimadzu, Japan) FTIR spectroscope with a scan step of 2 cm^{-1}.

2.2.5. Thermoelectric properties were investigated with an E502 analog-to-digital converter (LCARD, Russia). The hot end temperature was controlled with a PC-controlled heating table, and the cold end temperature was controlled with a K-type commercial thermocouple and PM8248S digital multimeter (PeakMeter, China). Aluminum foil was placed on the heating table for electromagnetic shielding, and a polyimide sheet was used to isolate electrical contacts. The sizes of rGO/PET and rMOG/PET structures for the Seebeck coefficient determination were 50 × 5 mm^2. rGO/rMOG/PET thermocouple leg sizes were decreased to 50 × 3 mm^2 for the device miniaturization. An anodized aluminum radiator was used as a heat sink. Electrical contacts were made of Ag paste and Cu tape.

Seebeck coefficient was calculated according to the formula (1) and corrected to the initial electromotive force (EMF) at the equilibrium state:

$$S = \Delta V / \Delta T \tag{1}$$

where ΔV and ΔT – are the voltage and temperature differences between the hot and cold ends of the thermocouple, respectively. Seebeck coefficient measurements were conducted twice for the sample with a sequential increase of the hot end temperature by 10 °C. After the first measurement cycle, the sample was cooled to room temperature, the registration channel of an E502 analog-to-digital converter (ADC) (LCARD, Russia) was moved from the hot to the cold end, and after the second measurement cycle, the calculated Seebeck coefficients were averaged.

2.2.6. The breathing test was performed under room conditions with normal breathing at a mouth-thermocouple distance of 2 cm using the E502 ADC (LCARD, Russia).

2.2.7. The EGT performance was demonstrated using a Zurich MLFI Lock-in Amplifier (Zurich Instruments, Germany). The EGT channel dimensions were approximately 2 × 2 mm^2. Drain and source contacts were made with copper tape and conductive silver paste and encapsulated with polydimethylsiloxane (PDMS). The applied drain-source voltage (V_{DS}) was 0.5 V, and the gate-source voltage (V_G) sweep rate was 25 mV/s. Transfer characteristics were recorded in the V_G range from −0.6 to +0.6 V. Pt wire was used as a gate electrode. A 20 μL drop of 0.1 M KCl was deposited on the EGT channel, and the transfer curve was recorded immediately. The following measurements were completed within 3 min.

2.2.8. Electrochemical treatment of the rGO/PET and rMOG/PET was performed in 20 μL of phosphate-buffered saline PBS (pH=6.86), and a potential of −4 V was applied for 200 s. Pt wire was used as a counter electrode. After the treatment, the samples were washed with deionized water and dried at 50 °C.

2.2.9. X-ray photoelectron spectroscopy was performed using a Thermo Fisher Scientific XPS NEXSA spectrometer with a monochromated Al K Alpha X-ray source at 1486.6 eV. The survey spectra were recorded with the pass energy of 200 eV and an energy resolution of 1 eV. For the high-resolution spectra, pass energy was 50 eV, and the energy resolution was equal to 0.1 eV. The spot area was 400 μm^2. A flood gun was used to compensate for sample charging.

3. Results and discussions

3.1. Materials characterization

Laser processing of GO on a polymer substrate enables both reduction and composite formation processes [10]. Laser irradiation induces photochemical and photothermal processes in GO and removes functional groups from the material, partly restoring graphene's electrical conductivity. The local temperature under the laser spot can reach 500

°C [24], melting the substrate's upper layer and driving rGO-polymer intermixing with further consolidation and formation of a conductive rGO/polymer composite. We implement this approach to produce flexible conductive structures, rGO/PET and rMOG/PET, following similar fabrication protocols and the same laser regime.

The conductivity type, charge mobility (μ), bulk charge concentration (ρ), and sheet resistance (R_s) were measured using a Hall effect measurement system. The majority of charge carriers for rGO/PET and rMOG/PET are holes with μ_h equal to (84 ± 2) $cm^2 V^{-1} s^{-1}$ and electrons with μ_e of (22 ± 3) $cm^2 V^{-1} s^{-1}$, respectively (Fig. 1a). ρ for rGO/PET is one order of magnitude lower than rMOG/PET values: $(8.6 \pm 0.4)\cdot 10^{17}$ vs. $(5.3 \pm 0.4)\cdot 10^{18}$ cm^{-3}, which explains the R_s difference for these samples, shown in Fig. 1b: (30.0 ± 0.5) and (18.3 ± 0.9) Ohm sq^{-1}. The higher charge density of rMOG compensates for lower charge mobility and improves conductance with respect to rGO. At the same time, both rGO and rMOG samples processed on glass show p-type conductivity with μ_h (69 ± 1) and (13 ± 1) $cm^2 V^{-1} s^{-1}$, respectively. R_s for rGO/glass and rMOG/glass were measured at (4.8 ± 0.2) kOhm sq^{-1} and (127.3 ± 0.1) Ohm sq^{-1}, which reveals the impact of the PET substrate on the material's electronic properties during laser processing. Notably, applying different processing conditions like laser regime and Ar atmosphere, we could not change the p-type conductivity of rGO/PET (Fig. S1). It became possible by replacing the graphene precursor with MOG, and only for PET substrates. To explain the unexpected result of the conductivity type transformation, we comprehensively analyzed the physicochemical properties of the produced materials on PET surfaces.

SEM images of processed materials (Fig. 1c, d) significantly differ from initial substances (Fig. S2): uniform flake distribution of GO and MOG on PET reconstructs into a complex 3D-structured rGO/PET and rMOG/PET with smooth coating. Raman spectra of GO and MOG films are represented by two conventional D and G peaks near 1350 and 1600 cm^{-1} with D/G ratios of 0.96 and 1.14, respectively. After laser processing, Raman spectra of rGO/PET and rMOG/PET transform to fluorescence signal (Fig. 1e) and reveal the coating of both samples by PET

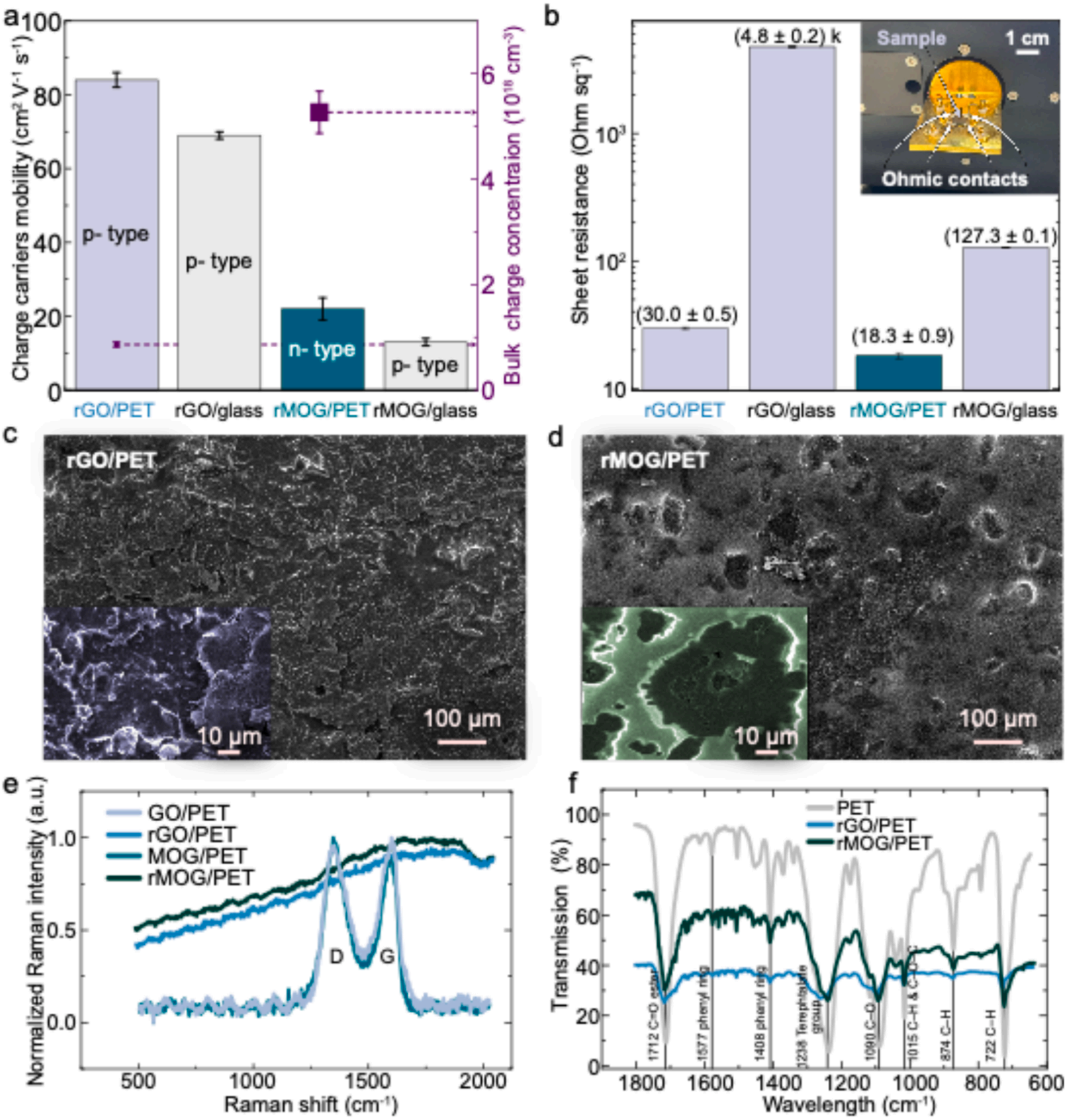

Fig. 1. (a) Charge carriers mobility and the bulk charge concentration for a set of samples: rGO/PET, rGO/glass, rMOG/PET, and rMOG/glass; (b) Sheet resistance of the samples in the logarithmic scale with the Hall measurement setup in the inset; (c, d) SEM images of rGO/PET and rMOG/PET; (e,f) Raman and FTIR spectra for the set of samples.

[25]. FTIR spectra in the fingerprint region (Fig. 1f) show PET modes for rGO/PET and rMOG/PET. The main bands are located at 722 (C–H), 874 (C–H), 1015 (C–H and C–O–C), 1090 (C–O), 1238 (terephthalate group), 1408 and 1577 (phenyl ring vibrations), and 1712 (C=O in esters) cm^{-1}. In other words, PET appears to dominate the signal of both composites in Raman and FTIR measurements, preventing us from discovering the origin of different conductivity types.

Being excited to find out the origin of p- and n-type conductivity, we implemented XPS analysis. C1s regions of both rGO/PET and rMOG/PET are characterized by CC sp^2 (284.0 eV), CC sp^3 (284.7 eV), C–O (286.4 eV), C=O (288.7 eV) bands with similar ratios as shown in Fig. S3. O1s region is represented by C=O and C–O bands near 532.0 and 532.6 eV respectively. The deconvoluted C1s region of rGO/PET differs significantly across the single sample. This is explained by the heterogeneity of the morphology and composition of the composite, where two components (rGO and PET) are unevenly distributed, as seen in Fig. 1c, d. Deconvoluted spectra of rMOG/PET are reproducible; however, the PET part of the conductive network has to be considered. High heterogeneity and PET presence in the samples make a detailed analysis impossible. To facilitate the analysis of materials without PET interference, we used electrochemical (EC) treatment to remove PET from the surface (ECrGO/PET, and ECrMOG/PET samples), as was shown in our previous work [26]. A constant voltage of −4 V was applied to the rGO/PET and rMOG/PET electrodes for 200 s in the PBS solution. As a result, the ECrGO/PET and ECrMOG/PET samples were fabricated. Their SEM and optical images in Fig. 2a, 2b, and Fig. S4 confirm polymer coating erosion, while XPS spectra across the sample become identical (Fig. 2c, d, and Fig. S5). According to the Hall measurement results, the conductivity type of rGO and rMOG-based samples after EC treatment remains p- and n-type, respectively. Since O1s region spectra (Figs. S5c and S5d) are not commonly used to estimate bond content [27,28], we focused on the analysis of the C1s region. Fitted spectra of C1s region of ECrGO/PET and ECrMOG/PET in Fig. 2c and 2d demonstrate four prominent bands related to CC sp^2 (284.0 and 284.1 eV), CC sp^3 (284.6 and 284.5 eV), C–O (286.2 and 286.0 eV), and C=O (288.5 and 288.4 eV), respectively. The atomic concentrations of C–O and C=O bands in ECrGO/PET are 8.2 and 4.5 %, while for ECrMOG/PET they are 3.3 and 1.3 %, respectively.

Higher content of the oxygen-containing groups for ECrGO/PET is also expected from the fact that the GO has more carbonyl and C–O groups than MOG as can be seen from the XPS spectra of initial precursors presented in Fig. S6. Namely, the C–O and C=O atomic concentrations are equal to 16.7 and 4.2 % for GO, and 6.7 and 4.3 % for MOG, respectively. Higher content of oxygen in the rGO system contributes to withdrawing electron density from the carbon network due to electronegative oxygen and results in different conductivity types of rGO/PET and rMOG/PET.

3.2. Applications

3.2.1. Thermocouple

The combination of p- and n-type materials could be used in thermocouple (TC) applications due to the opposite sign of their Seebeck coefficient, which enhances the device's sensitivity. The implementation of p-/*n*- junction enables electrons and holes to drift from the hot to the cold end in opposite directions simultaneously. As a result, the induced thermal electromotive force (EMF) is enhanced by summing the opposite charges on the cold end. First, we measured the thermal EMF of rGO/PET and rMOG/PET structures. A sketch of the experimental setup is shown in Fig. 3a. The EMF as a function of temperature for rGO/PET and rMOG/PET samples is shown in Fig. 3b Seebeck coefficients (S) for rGO/PET and rMOG/PET were estimated as (6.6 ± 1.4) and (−3.9 ± 0.8) μV K^{-1}, respectively. Upon heating, the charge carriers diffuse to the cold end of the structure. Holes for rGO/PET and electrons for rMOG/

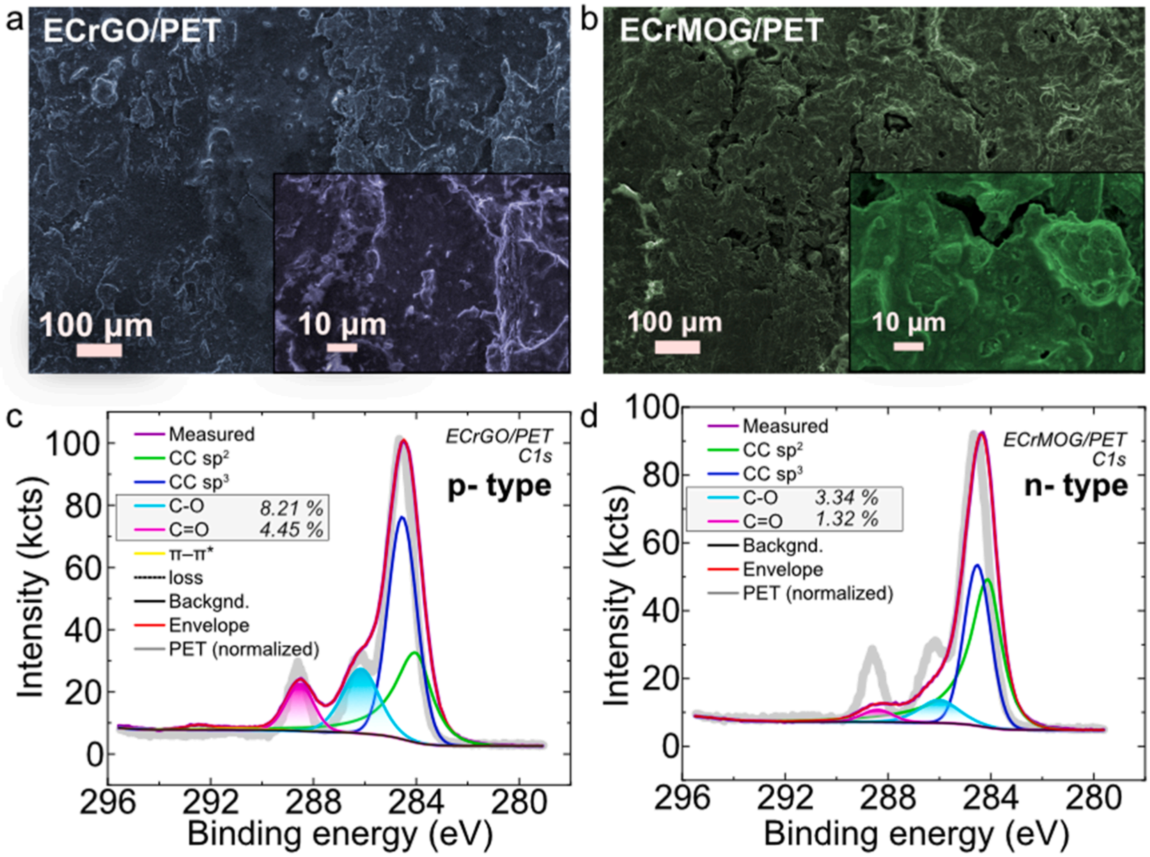

Fig. 2. (a,b) SEM images of ECrGO/PET and ECrMOG/PET; (c,d) Deconvoluted XPS spectra of C1s regions of ECrGO/PET and ECrMOG/PET.

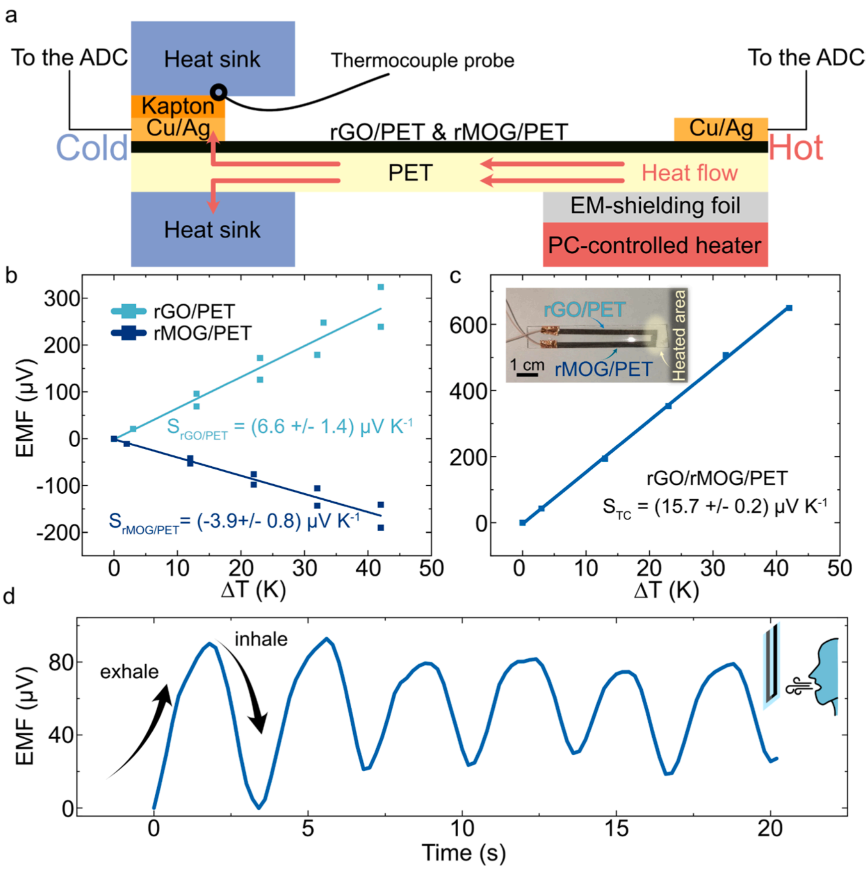

Fig. 3. (a) Seebeck coefficient measurement experimental setup; (b) EMF plot for the rGO/PET and rMOG/PET; (c) The performance of rGO-rMOG/PET thermocouple; (d) Response of the TC to the breathing under room conditions.

PET are majority carriers that accumulate on the cold end and create a potential difference reflected in the Seebeck coefficient, positive for the p-type and negative for the n-type material, confirming the Hall measurements.

We exploited these materials' properties to fabricate a flexible thermocouple on PET with an rGO-rMOG junction. It operates in the temperature range of PET stability (up to 70 °C), confirmed by the TC resistance consistency at these temperatures (Fig. S7). The sensitivity of the device was (15.7 ± 0.2) μV K^{-1} (Fig. 3c), which is on par with the state of the art of all-carbon flexible TCs [29,30]. Notably, the sensitivity could be increased by reducing the TC resistance, for example, by scaling the width of the rGO and rMOG legs (Fig. S8). Using our device, we could track human breathing with 50 μV changes due to periodic temperature oscillations (Fig. 3d).

Despite the successful design of TC, it was impossible to fabricate a p-n diode. To understand the possible reason, we investigated the morphology of TC interfaces. The scheme describing the thermocouple structure and the region of interest is presented in Fig. S9. Materials interconnections were analyzed by SEM at three locations: rGO/PET – rGO/rMOG/PET overlap (1), rGO/rMOG/PET overlap (2), and rGO/rMOG/PET overlap – rMOG/PET (3). The results demonstrated a blurred interface with blended components that do not properly separate p- and n-type zones and limit depletion region formation.

3.2.2. *Electrolyte-gated transistor*

Since the structures are mechanically robust and flexible [10], the confirmed conductivity type difference of the rGO- and rMOG/PET composites under the same processing conditions inspired us to explore the applicability of these materials in advanced electronics. One of the most attractive applications is flexible electrolyte-gated transistors (EGTs). The EGT working principle is based on the modulation of charge carriers in the channel by the potential of a gate electrode (V_G) immersed in electrolyte [31]. EGTs are commonly used in bioelectronics because of their high sensitivity, signal amplification ability [32], and low operating voltage, not exceeding 1 V [33].

We compared the electron-hole modulation in rGO/PET and rMOG/PET. The transfer characteristics of rGO/PET and rMOG/PET with negligible current (I_D) modulation were recorded, as shown in Fig. S10. We explain these results as due to polymer shielding suppressing the EGT working mechanism. EC-treated rGO/PET and rMOG/PET samples demonstrate h^+- and e$^-$-modulation within the V_G bias range from −0.6 to +0.6 V (green lines in Fig. 4a, b), revealing the presence of both charge carrier types. Transconductance (g_m) was calculated as the slope of a linear region of the IV transfer curve. The hole transconductances (g_m^h) were 29 and 27 μS for ECrGO/PET and ECrMOG/PET, respectively. In comparison, the electron transconductances (g_m^e) were 68 and 81 μS, with the Dirac point at 0.21 and 0.15 V, respectively.

Nevertheless, we discovered a p- to n-type transition for the ECrGO/PET and ECrMOG/PET samples during the EGT testing, presented in Fig. 4a and 4b Transfer characteristics were recorded for 3 min between scans. We observe consistent g_m^h decrease and rise of g_m^e for both ECrGO/PET and ECrMOG/PET. For ECrGO/PET and ECrMOG/PET, g_m^h drops to 20 and 19 μS, respectively. In comparison, g_m^e increases to 73 μS for ECrGO/PET and to 140 μS for ECrMOG/PET (Fig. 4c). Moreover, the Dirac point shifts to −0.06 V and −0.11 V for ECrGO/PET and ECrMOG/PET, respectively (Fig. 4d). To understand the origin of these changes and check their reversibility, we rinsed the samples with distilled water to wash out potassium, dried them on a heating plate at 50 °C, and reproduced the experiment. We observed the same behavior with g_m changes and the Dirac point downshift (Fig. S11).

The reason for the p- to n-type conductivity change in ECrGO/PET is still debated. Some works reported that oxidation or a lower degree of

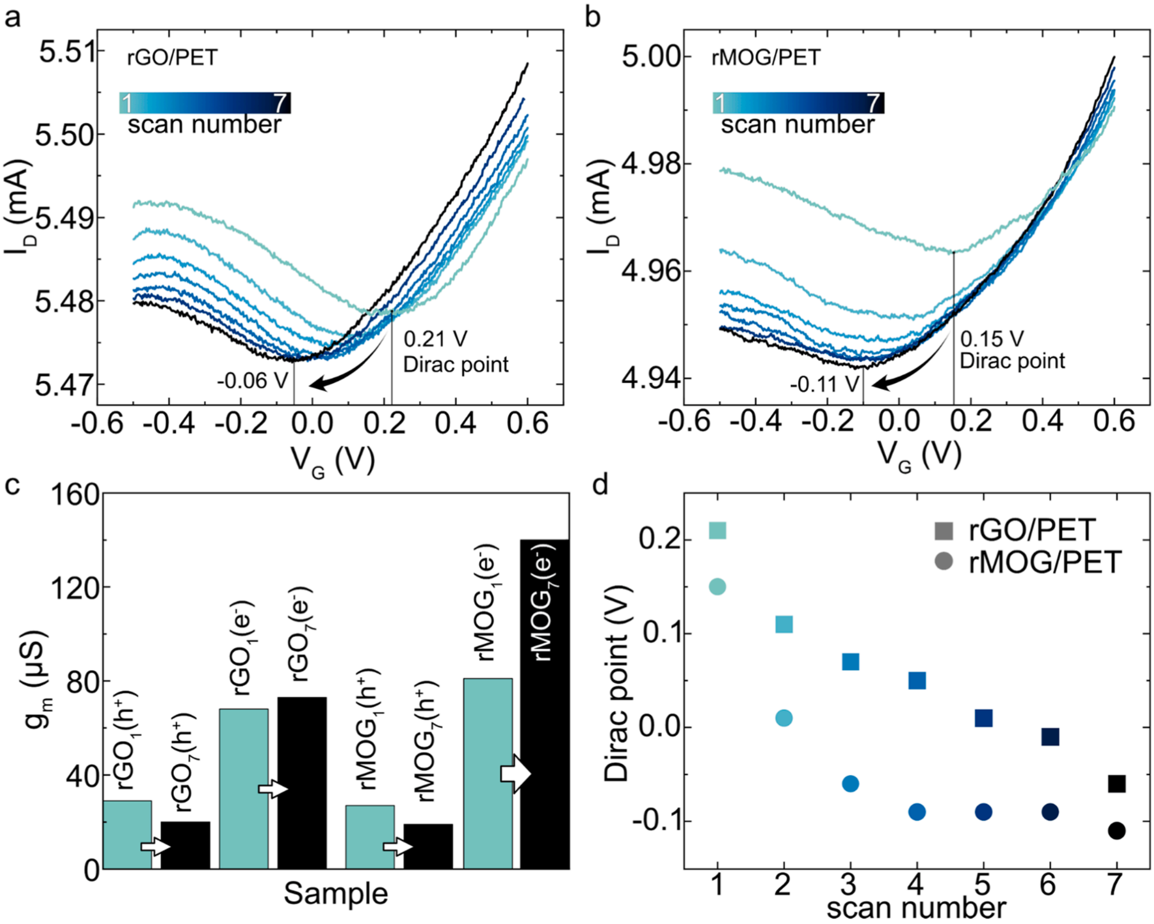

Fig. 4. Time-dependent transfer characteristic of (a) ECrGO/PET and (b) ECrMOG/PET; (c) Extracted transconductance for the 1st and the 7th scan for the ECrGO/PET and ECrMOG/PET. The scan number is labeled with a subscript index; (d) Dirac point for the ECrGO/PET and ECrMOG/PET at every cycle.

reduction promotes the p-type conductivity of rGO [19,34]. However, Bark et al. [2] observed the opposite effect in rGO thermally reduced in an Ar atmosphere, Dirac point downshift, and electron mobility increase as the degree of reduction decreased. Other studies [20] reported different results for temperature-dependent p-n conversion of rGO. However, these studies did not investigate rGO properties in an EGT configuration, and annealing was performed in an N_2 atmosphere. Based on these conflicting results, we conclude that the conductivity type strongly depends on the reduction method, whether electrochemical or thermal annealing and the environmental conditions under Ar or N_2 atmospheres.

However, these previous works cannot explain the rGO evolution we observe. The applied gate potential is insufficient for water electrolysis. Thus, we do not expect the formation of OH$^-$ ions, which could affect the EGT performance as oxygen-containing groups. Therefore, we propose a different p- to n-transition mechanism. Devices operating on this principle are known as electrochemical transistors (ECTs). ECTs are a type of EGTs that operate by modulating the drain current by ions in the electrolyte, which can migrate into the channel [35,36]. ECTs are typically made of organic polymers like PEDOT or polypyrrole [37], while rGO channels commonly work in the EGT regime [22,38].

To investigate the ECT mechanism and the impact of electrochemical reactions, we applied 0.1 M KCl solution to the rGO channel and left it for 20 min without applying V_{DS} and V_G (both equal zero). After that, we measured the transfer characteristics within a 3-minute interval (Fig. S12). The first scan reveals the stability of our EGTs in KCl water solution with a positive Dirac point near 0.2 V, while further sweeps demonstrate an n-type transition. Moreover, we found that positive bias promotes p- to *n*- transition more effectively than negative V_G. We applied $V_G = -0.6$ and $+0.6$ V for 1 min with measurements after each cycle. After polarization with a negative bias, the Dirac point was not shifted. Still, the cycle with positive V_G resulted in a Dirac point downshift from -0.05 to -0.11 V. This phenomenon could be explained by either EC reactions in rGO/PET changing redox state or the channel doping by K^+. Considering the absence of reduction and oxidation peaks within the operating V_{DS} and V_G range in both transfer and output characteristics (Fig. S13), we conclude that K^+ doping is the most likely dominating mechanism. Potassium ions penetrate the channel and redistribute the electron density around oxygen (C–O and C=O groups), reducing its electronegativity relative to carbon. K ions make C–O/C=O groups less electron-withdrawing, leading to n-type conductivity. The higher ionic radius of Cl$^-$ prevents channel penetration and blocks the opposite mechanism of increasing the electronegativity of C=O/C-O groups. Notably, the device could be restored to its original state by washing and drying at 50 °C, while the EC method was ineffective. This again confirms that no EC reactions occurred. These findings show that rGO can serve as an ECT active material, where its conductivity type can be tuned via ion doping, opening up new possibilities for (bio)sensing and the easy fabrication of ion-selective graphene-based transistors.

4. Conclusion

In this work, we demonstrated the fabrication of p- and n-type flexible carbon-based conductive composites using laser processing of GO and MOG on PET substrates, respectively. We investigated their physicochemical properties and established the significant role of graphene functionalization and polymer substrate for laser-processed precursor transformation. The higher concentration of GO's C=O and C–O groups allows fabricating p-type composites. Meanwhile, using graphene with a lower oxidation degree promotes the formation of an n-type material at the same laser power. This approach enabled the fabrication of p-n conjugated structures for flexible electronics applications such as thermocouples with a sensitivity of 18 μV K^{-1}, comparable to laser-processed copper/constantan thermocouples [39]. Additional electrochemical processing of the composites activated the surface for use as a transistor channel. The electrolyte-gated transistors showed ambipolar behavior with an unconventional p- to n-type transition attributed to ion doping. This transition occurred within the water window, allowing stable n-type graphene/polymer liquid-gated transistors to be fabricated, promising for (bio)sensing applications.

CRediT authorship contribution statement

Ilia Petrov: Writing – original draft, Visualization, Validation, Methodology, Investigation, Formal analysis, Data curation. **Dmitry Cheshev:** Writing – original draft, Validation, Software, Investigation. **Sergey Kaprov:** Writing – original draft, Software, Data curation. **Fedora Vasileva:** Writing – original draft, Methodology, Data curation. **Raul D. Rodriguez:** Writing – review & editing, Supervision, Conceptualization. **Evgeniya Sheremet:** Writing – review & editing, Supervision, Resources, Project administration, Funding acquisition, Conceptualization.

Declaration of competing interest

The authors declare that they have no known competing financial interests or personal relationships that could have appeared to influence the work reported in this paper.

Acknowledgements

The work was supported by the Russian Science Foundation grant № 22-12-20027, https://rscf.ru/project/22-12-20027/, and funding from the Tomsk region administration “Electronic components based on laser integration for the biocompatible/biodegradable flexible electronic devices”.

The authors are grateful to the center of TPU’s “Physical and chemical methods of analysis” and Kogolev D.A. for XPS measurements.

Supplementary materials

Supplementary material associated with this article can be found, in the online version, at doi:10.1016/j.surfin.2025.106666.

Data availability

Data will be made available on request.

References

[1] K.S. Novoselov, A.K. Geim, S.V. Morozov, D. Jiang, Y. Zhang, S.V. Dubonos, I. V. Grigorieva, A.A. Firsov, Electric field effect in atomically thin carbon films, Science 306 (2004) 666–669.

[2] H. Bark, M. Ko, M. Lee, W. Lee, B. Hong, H. Lee, Thermoelectric properties of thermally reduced graphene oxide observed by tuning the energy states, ACS Sustain. Chem. Eng. 6 (2018) 7468–7474.

[3] S. Tang, W. Wu, X. Xie, X. Li, J. Gu, Band Gap Opening Of Bilayer Graphene by Graphene Oxide Support Doping, 7, RSC Adv, 2017, pp. 9862–9871.

[4] S.N. Alam, N. Sharma, L. Kumar, Synthesis of graphene oxide (GO) by modified hummers method and its thermal reduction to obtain reduced graphene oxide (rGO), Graphene 06 (2017) 1–18.

[5] A. Jiříčková, O. Jankovský, Z. Sofer, D. Sedmidubský, Synthesis and applications of graphene oxide, Materials (Basel) (2022) 15, https://doi.org/10.3390/ma15030920.

[6] A. Lipovka, I. Petrov, M. Fatkullin, G. Murastov, A. Ivanov, N.E. Villa, S. Shchadenko, A. Averkiev, A. Chernova, F. Gubarev, M. Saqib, W. Sheng, J.-J. Chen, O. Kanoun, I. Amin, R.D. Rodriguez, E. Sheremet, Photoinduced flexible graphene/polymer nanocomposites: design, formation mechanism, and properties engineering, Carbon N. Y. 194 (2022) 154–161.

[7] F. Vasileva, V. Popov, I. Antonova, S. Smagulova, Screen-printed structures from a highly conductive mildly oxidized graphene suspension for flexible electronics, Materials (Basel) (2022) 15, https://doi.org/10.3390/ma15031256.

[8] R. Tarcan, O. Todor-Boer, I. Petrovai, C. Leordean, S. Astilean, I. Botiz, Reduced graphene oxide today, J. Mater. Chem. C Mater. Opt. Electron. Devices 8 (2020) 1198–1224.

[9] V. Agarwal, P.B. Zetterlund, Strategies for reduction of graphene oxide – A comprehensive review, Chem. Eng. J. 405 (2021) 127018.

[10] E. Abyzova, I. Petrov, I. Bril’, D. Cheshev, A. Ivanov, M. Khomenko, A. Averkiev, M. Fatkullin, D. Kogolev, E. Bolbasov, A. Matkovic, J.-J. Chen, R.D. Rodriguez, E. Sheremet, Universal Approach to Integrating Reduced Graphene Oxide into Polymer Electronics, Polymers (Basel) (2023) 15, https://doi.org/10.3390/polym15244622.

[11] K.-Y. Hwa, R. Murugan, S.-F. Tseng, A. Santhan, J.-Y. Lin, Laser-induced reduced graphene oxide for high-performance electrochemical sensors of antipyretic drug in real samples, Environ. Sci. Nano 11 (2024) 951–968.

[12] B. Sindhu, A. Kothuru, P. Sahatiya, S. Goel, S. Nandi, Laser-induced graphene printed wearable flexible antenna-based strain sensor for wireless human motion monitoring, IEEE Trans. Electron Devices 68 (2021) 3189–3194.

[13] J.-H. Lee, K. Cho, J.-K. Kim, Age of flexible electronics: emerging trends in soft multifunctional sensors, Adv. Mater. 36 (2024) e2310505.

[14] F. Schedin, A.K. Geim, S.V. Morozov, E.W. Hill, P. Blake, M.I. Katsnelson, K. S. Novoselov, Detection of individual gas molecules adsorbed on graphene, Nat. Mater. 6 (2007) 652–655.

[15] L. Wang, Y. Park, P. Cui, S. Bak, H. Lee, S.M. Lee, H. Lee, Facile preparation of an n-type reduced graphene oxide field effect transistor at room temperature, Chem. Commun. 50 (2014) 1224–1226.

[16] Y.-S. Chang, F.-K. Chen, D.-C. Tsai, B.-H. Kuo, F.-S. Shieu, N-doped reduced graphene oxide for room-temperature NO gas sensors, Sci. Rep. 11 (2021) 20719.

[17] S. Horike, Q. Wei, K. Akaike, K. Kirihara, M. Mukaida, Y. Koshiba, K. Ishida, Bicyclic-ring base doping induces n-type conduction in carbon nanotubes with outstanding thermal stability in air, Nat. Commun. 13 (2022) 3517.

[18] D. Wei, Y. Liu, Y. Wang, H. Zhang, L. Huang, G. Yu, Synthesis of N-doped graphene by chemical vapor deposition and its electrical properties, Nano Lett. 9 (2009) 1752–1758.

[19] Y. Sato, K. Takai, T. Enoki, Electrically controlled adsorption of oxygen in bilayer graphene devices, Nano Lett. 11 (2011) 3468–3475.

[20] N.D.K. Tu, J. Choi, C.R. Park, H. Kim, Remarkable conversion between n- and p-type reduced graphene oxide on varying the thermal annealing temperature, Chem. Mater. 27 (2015), https://doi.org/10.1021/acs.chemmater.5b02999.

[21] A. Bhaumik, J. Narayan, Conversion of p to n-type reduced graphene oxide by laser annealing at room temperature and pressure, J. Appl. Phys. 121 (2017) 125303.

[22] R. Furlan de Oliveira, P.A. Livio, V. Montes-García, S. Ippolito, M. Eredia, P. Fanjul-Bolado, M.B. González García, S. Casalini, P. Samorì, Liquid-gated transistors based on reduced graphene oxide for flexible and wearable electronics, Adv. Funct. Mater. 29 (2019) 1905375.

[23] F.D. Vasilieva, A.N. Kapitonov, E.A. Yakimchuk, S.A. Smagulova, I.V. Antonova, I. A. Kotin, Mildly oxidized graphene oxide suspension for printing technologies, Mater. Res. Express 5 (2018) 065608.

[24] Y. Huang, D. Ma, P. Turner, G.E. Donnelly, J.M. Katzen, W.R. Hendren, J.M. Gregg, R.M. Bowman, L. Zhang, G. Zhang, F. Huang, Customizing the reduction of individual graphene oxide flakes for precise work function tuning with meV precision, Nanoscale Adv. 2 (2020) 2738–2744.

[25] I. Petrov, R.D. Rodriguez, E. Frantsina, A. Grinko, E. Sheremet, Transforming oil waste into highly conductive composites: enabling flexible electronics through laser processing of asphaltenes, Adv. Compos. Hybrid Mater. 7 (2024), https://doi.org/10.1007/s42114-024-00855-0.

[26] M. Fatkullin, I. Petrov, E. Dogadina, D. Kogolev, A. Vorobiev, P. Postnikov, J.-J. Chen, R.F. de Oliveira, O. Kanoun, R.D. Rodriguez, E. Sheremet, Electrochemical switching of laser-induced graphene/polymer composites for tunable electronics, Polymers (Basel) (2025) 17, https://doi.org/10.3390/polym17020192.

[27] T.R. Gengenbach, G.H. Major, M.R. Linford, C.D. Easton, Practical guides for x-ray photoelectron spectroscopy (XPS): interpreting the carbon 1s spectrum, J. Vac. Sci. Technol. A 39 (2021) 013204.

[28] D.V. Sivkov, O.V. Petrova, S.V. Nekipelov, A.S. Vinogradov, R.N. Skandakov, K. A. Bakina, S.I. Isaenko, A.M. Ob’edkov, B.S. Kaverin, I.V. Vilkov, V.N. Sivkov, Quantitative characterization of oxygen-containing groups on the surface of carbon materials: XPS and NEXAFS study, Appl. Sci. (Basel) 12 (2022) 7744.

[29] S. Kim, S. Lim, M.H. Jeong, W. Kim, S. Baik, J.W. Suk, Flexible thermocouple using a thermoelectric graphene fiber with a seamless junction, J. Mater. Sci. Technol. 172 (2024) 15–22.

[30] R. Mulla, C.W. Dunnill, Single material thermocouples from graphite traces: fabricating extremely simple and low cost thermal sensors, Carbon Trends 4 (2021) 100077.

[31] F. Torricelli, D.Z. Adrahtas, Z. Bao, M. Berggren, F. Biscarini, A. Bonfiglio, C. A. Bortolotti, C.D. Frisbie, E. Macchia, G.G. Malliaras, I. McCulloch, M. Moser, T.-Q. Nguyen, R.M. Owens, A. Salleo, A. Spanu, L. Torsi, Electrolyte-gated transistors for enhanced performance bioelectronics, Nat. Rev. Methods Primers 1 (2021), https://doi.org/10.1038/s43586-021-00065-8.

[32] R. Furlan de Oliveira, V. Montes-García, P.A. Livio, M.B. González-García, P. Fanjul-Bolado, S. Casalini, P. Samorì, Selective ion sensing in artificial sweat using low-cost reduced graphene oxide liquid-gated plastic transistors, Small 18 (2022) e2201861.

[33] S.H. Kim, K. Hong, W. Xie, K.H. Lee, S. Zhang, T.P. Lodge, C.D. Frisbie, Electrolyte-gated transistors for organic and printed electronics, Adv. Mater. 25 (2013) 1822–1846.

[34] S. Vasilijević, G. Mattana, G. Anquetin, N. Battaglini, B. Piro, Electrochemical tuning of reduced graphene oxide in printed electrolyte-gated transistors. Impact on charge transport properties, Electrochim. Acta 371 (2021) 137819.

[35] I. Gualandi, M. Tessarolo, F. Mariani, D. Arcangeli, L. Possanzini, D. Tonelli, B. Fraboni, E. Scavetta, Layered double hydroxide-modified organic electrochemical transistor for glucose and lactate biosensing, Sensors 20 (2020), https://doi.org/10.3390/s20123453.

[36] M. Clua Estivill, A. Ait Yazza, P. Blondeau, F.J. Andrade, Ion-selective organic electrochemical transistors for the determination of potassium in clinical samples, Sens. Actuators B Chem. 401 (2024) 135027.

[37] J. Rivnay, S. Inal, A. Salleo, R.M. Owens, M. Berggren, G.G. Malliaras, Organic electrochemical transistors, Nat. Rev. Mater. 3 (2018) 17086.

[38] M. Sensi, R.F. de Oliveira, M. Berto, M. Palmieri, E. Ruini, P.A. Livio, A. Conti, M. Pinti, C. Salvarani, A. Cossarizza, J.M. Cabot, J. Ricart, S. Casalini, M. B. González-García, P. Fanjul-Bolado, C.A. Bortolotti, P. Samorì, F. Biscarini, Reduced graphene oxide electrolyte-gated transistor immunosensor with highly selective multiparametric detection of anti-drug antibodies, Adv. Mater. 35 (2023) e2211352.

[39] M.T. Rahman, C.-Y. Cheng, B. Karagoz, M. Renn, M. Schrandt, A. Gellman, R. Panat, High performance flexible temperature sensors via nanoparticle printing, ACS Appl. Nano Mater 2 (2019) 3280–3291.